Acta Pharmaceutica Sinica B 2022;12(8):3354–3366

Chinese Pharmaceutical Association
Institute of Materia Medica, Chinese Academy of Medical Sciences

Acta Pharmaceutica Sinica B

www.elsevier.com/locate/apsb
www.sciencedirect.com

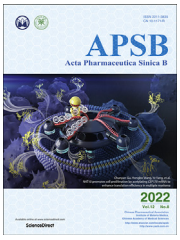

ORIGINAL ARTICLE

Dual-responsive nanoparticles with transformable shape and reversible charge for amplified chemo-photodynamic therapy of breast cancer

Wenfeng Jia[a,†], Rui Liu[a,†], Yushan Wang[a], Chuan Hu[a], Wenqi Yu[a], Yang Zhou[a], Ling Wang[a], Mengjiao Zhang[a], Huile Gao[a,*], Xiang Gao[b,*]

[a]*Key Laboratory of Drug-Targeting and Drug Delivery System of the Education Ministry, Sichuan Engineering Laboratory for Plant-Sourced Drug and Sichuan Research Center for Drug Precision Industrial Technology, West China School of Pharmacy, Sichuan University, Chengdu 610064, China*
[b]*Department of Neurosurgery and Institute of Neurosurgery, State Key Laboratory of Biotherapy, West China Hospital, West China Medical School, Sichuan University and Collaborative Innovation Center for Biotherapy, Chengdu 610041, China*

Received 20 January 2022; received in revised form 16 February 2022; accepted 21 February 2022

KEY WORDS

Shape transformation;
Charge reversal;
Chemo-photodynamic therapy;
Self-delivery;
MMP-2 response;
pH response;
Carrier-free nanoparticles;
Breast cancer

Abstract Herein, we designed a dual-response shape transformation and charge reversal strategy with chemo-photodynamic therapy to improve the blood circulation time, tumor penetration and retention, which finally enhanced the anti-tumor effect. In the system, hydrophobic photosensitizer chlorin e6 (Ce6), hydrophilic chemotherapeutic drug berberrubine (BBR) and matrix metalloproteinase-2 (MMP-2) response peptide (PLGVRKLVFF) were coupled by linkers to form a linear triblock molecule BBR-PLGVRKLVFF-Ce6 (BPC), which can self-assemble into nanoparticles. Then, positively charged BPC and polyethylene glycol-histidine (PEG-His) were mixed to form PEG-His@BPC with negative surface charge and long blood circulation time. Due to the acidic tumor microenvironment, the PEG shell was detached from PEG-His@BPC attributing to protonation of the histidine, which achieved charge reversal, size reduction and enhanced tumor penetration. At the same time, enzyme cutting site was exposed, and the spherical nanoparticles could transform into nanofibers following the enzymolysis by

*Corresponding authors. Tel./fax: +86 18780288069; +86 19983187916.
E-mail addresses: gaohuile@scu.edu.cn (Huile Gao), xianggao@scu.edu.cn (Xiang Gao).
[†]These authors made equal contributions to this work.

https://doi.org/10.1016/j.apsb.2022.03.010

MMP-2, while BBR was released to kill tumors by inducing apoptosis. Compared with original nanoparticles, the nanofibers with photosensitizer Ce6 retained within tumor site for a longer time. Collectively, we provided a good example to fully use the intrinsic properties of different drugs and linkers to construct tumor microenvironment-responsive charge reversal and shape transformable nanoparticles with synergistic antitumor effect.

1. Introduction

In recent years, although nanoparticles are widely used in tumor therapy[1], the tumor heterogeneity and complex tumor microenvironment seriously affect the distribution, penetration and retention of nanoparticles, attenuating antitumor effect[2–4]. The clearance by mononuclear phagocyte system (MPS) in the blood circulation makes it difficult for nanoparticles to enrich in the tumor site, the high interstitial fluid pressure in the tumor parenchyma tends to pump the nanoparticles back to the blood, and the dense matrix and high solid stress hinder the penetration of nanoparticles into deep tumors[5]. Therefore, it is important to overcome these barriers by designing novel nanoparticles, which has attracted increasing attention in the field[6–8].

Physical properties of nanoparticles, such as size[9], shape[10], and surface characteristics[11,12], play an important role in the tissue distribution, tumor penetration and retention. Generally, spherical nanoparticles have good tumor penetration, while nanofibers have good tumor retention[13]. Therefore, shape transformable nanoparticles are designed to overcome the shape controversial and improve intratumor drug delivery[14,15]. Matrix metalloproteinase-2 (MMP-2) is expressed excessively in breast cancer[16,17], which could specifically cleave the peptide PLGVR[18,19]. To enable MMP-2-responsive shape transformation, we designed a new peptide PLGVRKLVFF. In the peptide, KLVFF is derived from Aβ peptide, which can form β-sheet and finally construct nanofibers[20]. However, the proline (P) in the peptide can effectively inhibit β-sheet and thus inhibit the formation of nanofibers[21]. After introducing the hydrophobic head and hydrophilic tail into the PLGVRKLVFF peptide, the resulted linear molecule can form spherical nanoparticles due to the hydrophobic force, and change to nanofibers under MMP-2 hydrolysis, improving the tumor retention of hydrophobic drug.

Carrier-free nanoparticles have very high drug loading capacity and could avoid materials-originated side effect, which have been the most promising strategy in the drug delivery[22]. Therefore, we proposed to select suitable drugs for shape transformable nanoparticle construction. Chlorin e6 (Ce6) is a widely used hydrophobic photosensitizer for photodynamic therapy (PDT)[23]. Berberrubine (BBR) is a hydrophilic and positively charged antitumor drug that can achieve anti-tumor effect through a variety of mechanisms, such as promoting apoptosis, and producing reactive oxygen species (ROS)[24]. So, the Ce6 and BBR were conjugated by PLGVRKLVFF peptide (BBR-PLGVRKLVFF-Ce6, BPC) to construct a linear molecule that can form spherical nanoparticles due to the hydrophobic force. The MMP-2-responsive shape transformable BPC nanoparticles showed positive surface charge, which could penetrate deep tumor by caveolae-mediated endocytosis and exocytosis[25–27].

Although the shape transformation strategy can effectively improve the retention and penetration of nanoparticles at the tumor site, positively charged nanoparticles tend to be cleared by MPS in blood circulation, which attenuating the tumor targeting delivery efficiency[28]. Therefore, charge reversal has become an effective strategy to improve blood circulation and tumor distribution. Because of the precise location, real-time monitoring, microenvironment response, and low toxicity, stimuli-responsive nano-based drug delivery systems have been a promising approach in treatments[29,30]. Due to the acidic tumor microenvironment, pH response become one of the common trigger conditions. To provide the BPC nanoparticles with pH-responsive charge reversal property, polyethylene glycol-histidine (PEG-His) was used to coat the BPC to form a negatively charged nanoparticle (PEG-His@BPC) due to the electrostatic adsorption. The negative charge of PEG-His@BPC make it have long blood circulation time. After reaching the tumor site, the histidine was protonated, and PEG was detached to expose the positively charged BPC for tumor penetration, and MMP-2-triggered shape transformation.

In this study, we designed a pH-responsive charge reversal and MMP-2-responsive shape transformable nanoparticle PEG-His@BPC. The spherical PEG-His@BPC with negative charge had long blood circulation time and could passively target to tumor tissue. Due to the protonation of histidine in acidic tumor microenvironment, PEG shell fell off, and the positively charged BPC was exposed with good tumor penetration. Simultaneously, the highly expressed MMP-2 cleaved the PLGVR fragment, and the external hydrophilic BBR was detached and released to promote tumor cell apoptosis. At the same time, due to the switch of hydrophilic-hydrophobic ratio and the β-folding formation, the remaining pep-Ce6 was reassembled into nanofibers, thus increasing the tumor retention and cellular uptake. Under laser irradiation, high levels of ROS induced by Ce6 could further induce tumor cell apoptosis, which has synergistic effect with BBR. Based on this dual-responsive shape transformation combination therapy, self-delivered PEG-His@BPC achieved enhanced chemo-photodynamic combinational therapy against breast cancer (see Scheme 1).

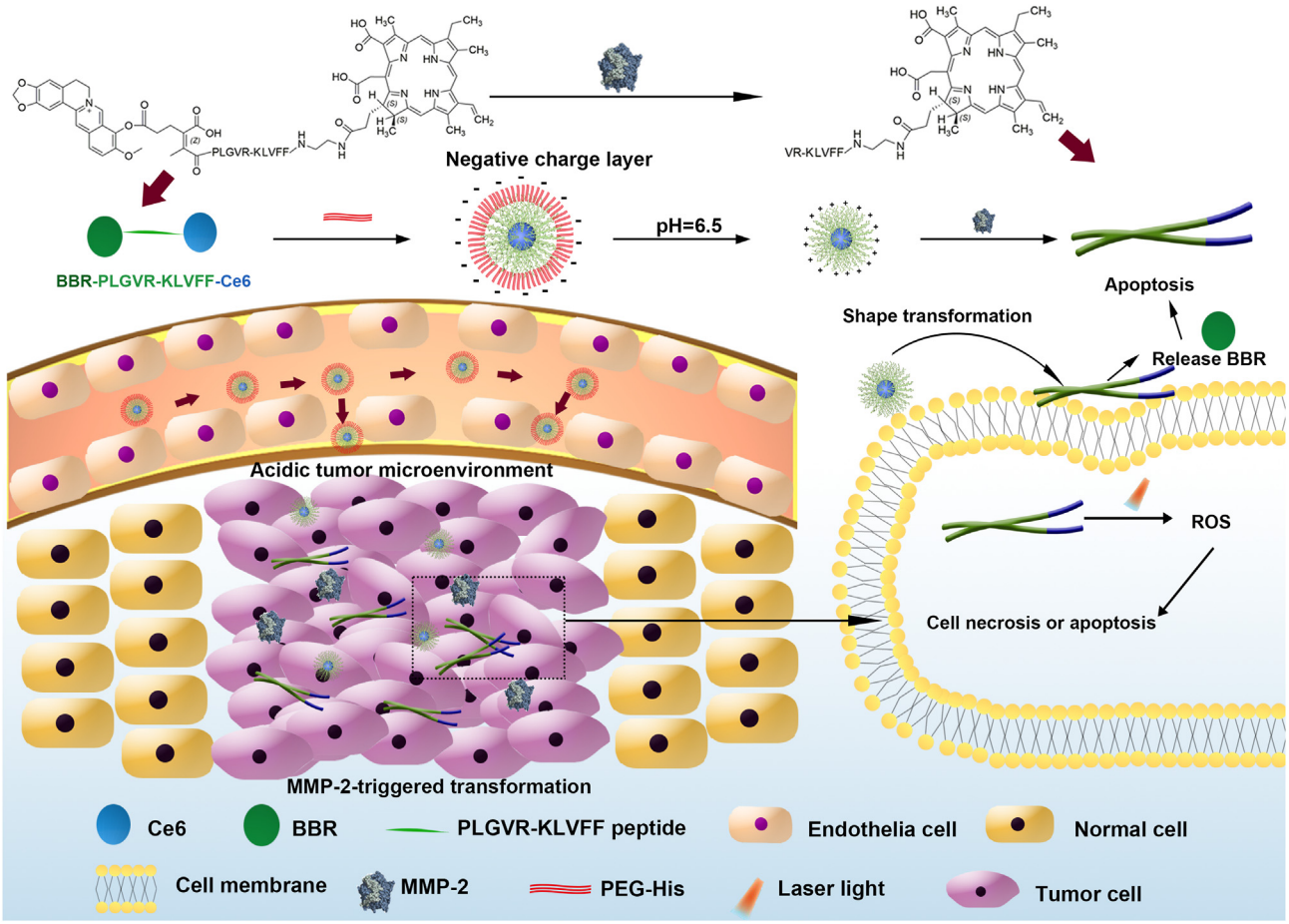

Scheme 1 Scheme illustration of the composition of PEG-His@BPC and its therapeutic effect on breast cancer.

2. Materials and methods

2.1. *Materials*

Fmoc-PLGVRK(Dde)LVFF (MW = 1561) was purchased from DECHI Biotechnology Co., Ltd. (Shanghai, China). Ce6 was purchased from Dalian Meilun Biotechnology Co., Ltd. (Dalian, China). BBR was purchased from PUFEIDE Biotechnology Co., Ltd. (Chengdu, China). CDM and *t*-butyloxy carbonyl (Boc)-ethylenediamine were purchased from McLean Biochemical Technology Co., Ltd. (Shanghai, China). Mouse 4T1 cells were obtained from the Cell Bank of Chinese Academy of Sciences (Shanghai, China). Cells were cultured in complete RPMI-1640 cell medium (YUANPEI, Shanghai, China) containing 10% fetal bovine serum, 100 U/mL penicillin G and 100 U/mL streptomycin sulfate. The cells were cultured at 37 °C and 5% CO_2. Female BALB/c mice (5−6 weeks, 18−22 g) and female BALB/c nude mice (4−5 weeks, 18 ± 2 g) were purchased from ENSI-WEIER Co., Ltd. (Chongqing, China). All animal experiments were conducted under the guidelines evaluated and approved by the Ethics Committee of Sichuan University.

2.2. *Synthesis of Ce6-NHNH$_2$*

Ce6 (3 mg) was dissolved in DMF (2 mL), then EDC·HCl (2.9 mg) and NHS (1.74 mg) were added to activate the carboxyl group. Then Boc-ethylenediamine (0.89 mg) was dissolved in DMF (1 mL) and mixed with Ce6. The mixture was stirred in darkness at room temperature (RT) for 12 h to obtain Boc-NHNH-Ce6. It was diluted to 6 mL with ultra-pure (UP) water, HCl was added to adjust pH to 6, and the solution was extracted 5 times with DCM. Then organic phase was merged, and the organic phase was washed with saturated NaCl solution to remove excess water-soluble impurities. DCM was removed by rotary evaporator, DCM and TFA (7:3) were added to remove the Boc under RT for 3 h. The DCM was removed by rotary evaporator again, and the salt of trifluoro-acetic acid was obtained. Then saturated $NaHCO_3$ solution was added to adjust pH to 8. After being extracted with DCM for 5 times, the organic phase was washed with saturated NaCl solution, and the organic phase was concentrated to obtain Ce6-NHNH$_2$.

2.3. *Synthesis of PLGVRK(Dde)LVFF-Ce6*

The Fmoc-PLGVRK(Dde)LVFF peptide (5 mg) was dissolved in 2 mL of DMF, and subsequently EDC·HCl (1.84 mg) and NHS (1.1 mg) were added to activate the carboxyl group. The solvent of Ce6-NHNH$_2$ solution was removed and 2 mL of DMF was added to dissolve Ce6-NHNH$_2$, and the solution was put into the activated peptide drop by drop. The mixture was stirred at RT and dark for 12 h. Then 20% 4-methylpiperidine was added to remove the Fmoc, and the mixture was dialyzed for 48 h. The dialysate was freeze-dried and finally PLGVRK(Dde)LVFF was obtained.

2.4. Synthesis of BBR-CDM

CDM (1.72 mg) was dissolved in 2 mL of anhydrous DCM at 0 °C, and oxalyl chloride (1.22 mg) and anhydrous DMF (1 μL) were added. The mixture was stirred in ice bath for 10 min and then stirred at RT for 1 h. Impurities such as DCM and excess oxalyl chloride were removed by rotary evaporation to get pure acyl chloride. BBR (3 mg), the above acyl chloride and anhydrous pyridine (2 μL) were mixed into anhydrous acetonitrile, and then the mixture was stirred at RT for 3 h to obtain BBR-CDM.

2.5. Synthesis of BPC and PEG-His

The PLGVRK(Dde)LVFF and BBR-CDM were dissolved in anhydrous DMF. Then 4-dimethylaminopyridine was added into the solution and the solution was stirred in darkness at RT for 12 h. Hydrazine hydrate solution (2%) was added to remove Dde, and then the BPC was purified by dialysis for 48 h. The mPEG-CM was dissolved in UP water, and EDC·HCl and NHS were added to activate carboxyl group for 3 h. Histidine was added into the mixture and the mixture was stirred for 24 h. Finally, PEG-His was purified by dialysis.

2.6. Preparation of PEG-His@BPC micelles

BPC was dissolved in chloroform:methanol (4:1) solvent, then 10-fold UP water volume was added. The mixed solvent was emulsified in ice water bath by ultrasonic emulsification (100 W, 5 min). Then organic solvent was removed by rotary evaporator, and the particle size of BPC micelles was measured by Malvern particle size analyzer (Malvern, Nano-ZS90, UK). Finally, the BPC micelles and PEG-His were incubated at RT for 12 h.

2.7. MMP-2-responsiveness

One milliliter of 0.5 mg/mL PEG-His@BPC was co-incubated with 300 ng/mL MMP-2 under pH 6.5 or 7.4, and groups without MMP-2 were used as control. The changes of particle size were monitored by Malvern particle size analyzer at 2, 4, 8 and 12 h.

2.8. Intracellular transformation

After discarding the culture medium, 2.5% glutaraldehyde fixation solution was added to the cultured 4T1 cells. Cells were fixed at RT for 5 min and then scraped off gently in one direction with cell scraper. The cell fluid was added to the centrifuge tube with Pasteur pipette and then centrifuged for 5 min. The supernatant fluid was discarded, and the fresh 2.5% glutaraldehyde fixed solution was added. The cell mass was gently picked up and suspended in the fixed solution. It was fixed away from light at RT for 30 min and then transferred to 4 °C for preservation. Finally, the fixed cells were made into ultra-thin sections and observed by TEM (JEOL, JEM-2100 Plus, Japan).

2.9. Penetration and retention in MSC

The low melting point agarose (2% *w*/*v*) was dissolved in the cell culture medium, and the solution was added to the 96-well plate (80 μL per well). After the gel was cooled and solidified, 4T1 cells were inoculated on the gel (3×10^3 cells per well) to formed MSC. The MSCs around 500 μm were selected and treated with PEG-His@BPC and PEG-His@BRC. After 12 h, MSCs were washed and fixed. Then the fluorescent intensity was observed by CLSM (ZEISS, LSM 800, Germany). Meanwhile, the medium was replaced with fresh culture medium and incubated for another 12 h. Then MSCs were washed and fixed, and the fluorescent intensity was observed to investigate the tumor retention of nanomedicines[31].

2.10. Calcein-AM/PI double staining

4T1 cells were inoculated on the 24-well plate. After being treated with different formulations for 12 h, 4T1 cells were washed and stained with Calcein-AM (5 μg/mL) and PI (10 μg/mL) for 30 min. Finally, 4T1 cells were washed to remove excess dyes and fluorescent intensity was observed by fluorescence microscope (Nikon, Ts2RFL, Japan).

2.11. Biodistribution

4T1 cells (4×10^5) were subcutaneously injected into the left mammary fat pads of female BALB/c nude mice. After 7 days, mice with tumor around 100 mm^3 were selected and randomly divided into 4 groups ($n = 3$), which were intravenously administrated with PEG-His@BPC, PEG-Phe@BPC, PEG-His@BRC and PEG-Phe@BRC, respectively. The *in vivo* fluorescence imaging was carried out at 4, 12, 24, 36 and 48 h post-intravenous administration by using the Lumina III imaging system (PerkinElmer, IVIS Lumina Series III, USA). All mice were sacrificed after the last imaging, and the major organs and tumors were cleaned, fixed and collected for *ex vivo* fluorescence imaging. All tumors and organs were dehydrated and frozenly sectioned, then imaged by CLSM (ZEISS). The scanning parameters of fluorescence imaging were as follows: excitation wavelength = 660 nm, emission wavelength = 710 nm, visual field = 12.5 cm, and fluency = 2 mW/cm^2. The camera is set to maximum gain and the split-box factor is 4, unless otherwise stated, the same below.

2.12. Retention in tumor

BALB/c nude mice 4T1 breast cancer model was constructed as above. One week later, mice with tumor around 100 mm^3 were selected and randomly divided into 4 groups ($n = 3$), which were intratumorally injected with PEG-His@BPC, PEG-Phe@BPC, PEG-His@BRC, PEG-Phe@BRC, respectively. The *in vivo* fluorescence imaging was detected at 0, 8, 12, 24 and 36 h after intratumoral injection. Then the *ex vivo* fluorescence imaging and fluorescent slices were made as before. In addition, tumors were made into ultra-thin sections and observed by TEM (JEOL).

2.13. Anti-tumor effect in vivo

BALB/c mice 4T1 breast cancer models were constructed as above. Six days later, mice with tumor around 80 mm^3 were selected and randomly divided into 9 groups ($n = 6$). Mice in different groups were intravenously injected with PBS, BBR, PEG-His@BPC, Ce6+L, PEG-His@BPC + L, PEG-Phe@BPC + L, PEG-His@BRC + L, PEG-Phe@BRC + L, PEG-His@APC + L (5 mg/kg Ce6 for each group), respectively.

The 650 nm laser irradiation was carried out at 24 h post-intravenous administration. The mice were treated every 3 days for 4 cycles, and the tumor volume and body weight were evaluated and recorded every 2 days from Day 6. All mice were sacrificed on Day 22 post-implantation of tumor, and major organs and tumors were cleaned, fixed and collected. The tumors were weighed and imaged in natural light. The sections prepared from tumors and organs were stained with H&E, Ki67 and TUNEL.

3. Results and discussions

3.1. Preparation and characterization of PEG-His@BPC

Mass spectrum showed that there were peaks at 639.0 and 320.0 (Supporting Information Fig. S1A), indicating the successful synthesis of Ce6−$NHNH_2$. The peak of m/z = 487.8 indicated the successful synthesis of BBR-2-(2-carboxyethyl)-3-methylmaleic anhydride (BBR-CDM, Fig. S1B). The peaks at 1796.2 and 2284.0 belonged to PLGVRKLVFF-Ce6 and BPC as detected by matrix-assisted laser desorption/ionization time-of-flight mass spectrometry (MALDI-TOF-MS, SHIMADZU, AXIMA-TOF, Japan), indicating the successful synthesis of BPC (Fig. 1A and B). The peaks at 5000.0 and 5145.4 belonged to PEG-CM and PEG-His, and the peak displacement of 150 indicated the successful synthesis of PEG-His (Fig. S1C and S1D). The average sizes of BPC micelles and PEG-His@BPC were 55.6 ± 4.3 and 76.7 ± 5.2 nm, respectively (Fig. 1C and D). When pH reduced from 7.4 to 6.5, the zeta potential of PEG-His@BPC converted from −13.5 ± 2.3 to 18.9 ± 1.7 mV (Fig. 1E), indicating the PEG-His could successfully detach from the particles at acidic condition.

3.2. MMP-2-responsiveness

PLGVR is not only a specific responsive peptide sequence of MMP-2[32], but also has the proline (P) which can effectively inhibit β-sheet and thus inhibit the formation of nanofibers. KLVFF, derived from Aβ peptide, often relies on a wide range of intermolecular hydrogen bonds to form β-sheet, which is easy to form nanofibers[20]. Therefore, the change of hydrophilic and hydrophobic force and release of proline inhibition caused by enzymatic hydrolysis can be used to re-form the β-sheet to realize the shape transformation from micelle to nanofiber. MALDI-TOF-MS (SHIMADZU) showed that the peak of PLGVRKLVFF changed obviously after MMP-2 cleavage, and the appearance of multiple peaks may be due to the results of multiple cleavage sites (Supporting Information Fig. S2A and S2B). On this basis, we co-incubated PEG-His@BPC with MMP-2 (denoted as + E) under pH 6.5 or 7.4, and groups without MMP-2 were used as control. The dynamic light scattering (DLS, Malvern) particle size of PEG-His@BPC + E at pH 6.5 changed most rapidly and strongly, which reached 2000 nm after 4-h incubation (Fig. 1F). This result indicated the nanoparticles could transform into nanofibers within 4 h. Moreover, transmission electron microscope (TEM, JEOL) showed that PEG-His@BPC had different shapes under different pH and MMP-2 conditions, and a large number of nanofibers appeared only in the presence of MMP-2 at pH 6.5 (Fig. 1G), indicating the PEG-His@BPC could successfully transform from spherical particles to nanofibers in the presence of MMP-2 and acidic condition[21,33,34]. In addition, DLS (Malvern) and TEM (JEOL) showed that enzymolysis of PEG-His@BPC by MMP-2 was slowed down under pH 7.4, but PEG-His@BPC could be quickly cleaved by MMP-2 and transformed into nanofibers under pH 6.5, which may be caused by the shedding of PEG shell at neutral condition.

3.3. Cellular uptake

Compared with PEG-His@BPC without MMP-2, the presence of MMP-2 obviously enhanced cellular uptake of PEG-His@BPC under pH 6.5 or 7.4 (1.67 and 1.35 times, respectively), according to both flow cytometry (Agilent, NovoCyte, USA, Fig. 2A) and confocal laser scanning microscopy (CLSM, ZEISS, Fig. 2B). The results demonstrated that the shape transformation can effectively promote the cellular uptake of nanoparticles, which was consistent with the previous reports[14]. Soft nanofibers are more likely to attach to the cell surface as they pass through the cell, rather than external cutting through it like spherical nanoparticles, so the difference in uptake capacity between nanofibers and micelles may be attributed to their stiffness[35].

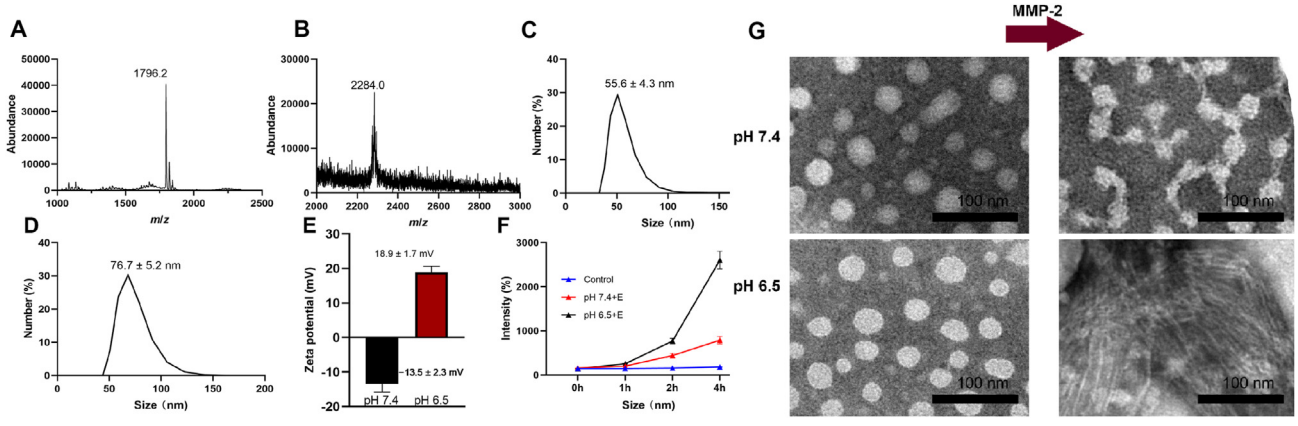

Figure 1 Characterizations of nanomedicines. The MALDI-TOF-MS (SHIMADZU) results of PLGVRKLVFF-Ce6 (A) and BPC (B). The DLS (Malvern) measurements of BPC (C) and PEG-His@BPC (D). (E) Zeta potentials of PEG-His@BPC in different pH values. Data are presented as mean ± SD (n = 3). (F) Size changes of PEG-His@BPC in different conditions. Data are presented as mean ± SD (n = 3). (G) TEM (JEOL) of PEG-His@BPC before and after being incubated with MMP-2 at pH 7.4 or 6.5.

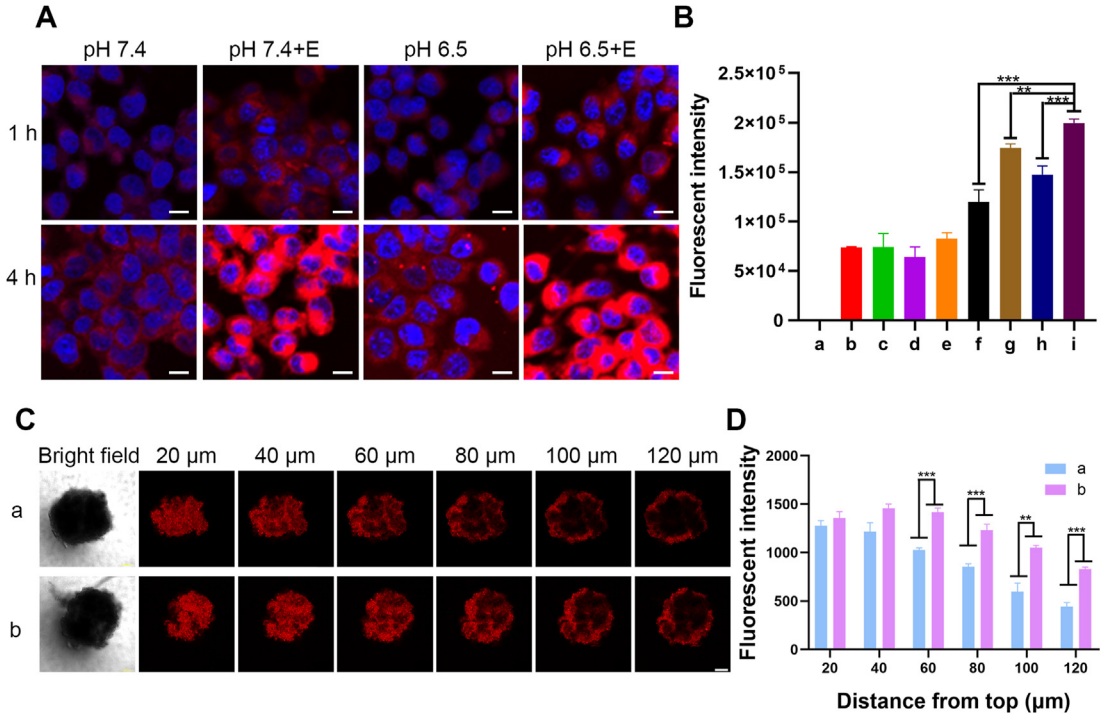

Figure 2 Cellular uptake and tumor retention of nanomedicines. 4T1 cells were incubated with different conditions for 1 or 4 h. Cellular uptake of nanomedicines was observed by (A) CLSM (ZEISS) and evaluated by (B) flow cytometry (Agilent). The a–i represent blank, 1 h pH 7.4, 1 h pH 7.4+E, 1 h pH 6.5, 1 h pH 6.5+E, 4 h pH 7.4, 4 h pH 7.4+E, 4 h pH 6.5, 4 h pH 6.5+E. Data are presented as mean ± SD ($n = 3$). Scale bars represent 20 μm. E represents MMP-2. (C) Confocal images of 4T1 MSCs incubated with (a) PEG-His@BRC and (b) PEG-His@BPC. Scale bar represents 100 μm. (D) Fluorescence semi-quantification of sections at different depth. Data are presented as mean ± SD ($n = 3$). $^{**}P < 0.01$ and $^{***}P < 0.001$ are considered as significant difference, respectively.

3.4. *Intracellular shape transformation*

First, we constructed a control peptide RPGFGNKLVFF that could not be cleaved by MMP-2, which displayed the same peaks before and after it incubated with MMP-2 as determined by MALDI-TOF-MS (SHIMADZU, Fig. S2A). Then we used the peptide to synthesize control nanoparticles PEG-His@BBR-RPGFGNKLVFF-Ce6 (PEG-His@BRC), which could not transform to nanofibers. Finally, we observed the shape transformation of PEG-His@BPC and PEG-His@BRC in 4T1 cells. As we expected, the results showed there were no nanofibers in cells treated with PEG-His@BRC, but plenty of spherical nanoparticles around 50 nm (blue arrow) were found in endosomes or cytoplasm (Supporting Information Fig. S3A). Importantly, the nanofibers (red arrow) were abundant in the cytoplasm of cells treated with PEG-His@BPC (Fig. S3B), indicating that PEG-His@BPC could transform from micelles to nanofibers at the cellular level, which was consistent with previous reports[36].

3.5. *Penetration and retention in multicellular spheroids*

The tumor penetration and retention of nanomedicines were confirmed by confocal imaging of multicellular spheroids (MSCs). First, the MSCs were treated with PEG-His@BRC and PEG-His@BPC for 12 h. There were similar Ce6 signals in PEG-His@BRC- and PEG-His@BPC-treated MSCs, suggesting that PEG-His@BPC displayed the same excellent penetration capacity as non-transformable spherical nanoparticles (Supporting Information Fig. S4A and S4B). Then each group of nanomedicines was replaced with fresh culture medium and incubated for another 12 h to investigate the tumor retention of nanomedicines. The results showed PEG-His@BRC was excreted rapidly, which tended to vanish at 80 μm. In contrast, there were strong Ce6 signals retained in the MSCs treated with PEG-His@BPC (Fig. 2C). The fluorescence signals of PEG-His@BPC group were 1.87-fold higher than that of PEG-His@BRC group at 120 μm of depth, indicating PEG-His@BPC displayed better tumor retention than non-transformable PEG-His@BRC (Fig. 2D). Meanwhile, the difference between MSCs treated with PEG-His@BRC and PEG-Phe@BRC was compared to confirm the contribution of charge reverse in spheroids penetration (Fig. S4C and S4D). The results showed that fluorescence intensity of PEG-His@BRC was 1.33-fold higher than that of PEG-Phe@BRC at 120 μm of depth, which proved that the charge reversal was beneficial to the tumor penetration. A good tumor penetration achieved by charge reversal could enrich more nanoparticles in the deep part of the tumor, which could cooperate with the enhancement of tumor retention caused by shape transformation to enhance the delivery efficiency. Solid tumor simulation well proved that PEG-His@BPC could first show good tumor penetration, and then retain in deep tumor for a longer time, which was consistent with the previous reports[37,38].

3.6. *ROS generation*

First, we synthesized PEG-Phe@BPC as control nanoparticles, in which the histidine of PEG-His@BPC was replaced by phenylalanine (Phe). The PEG-Phe@BPC could not remove the PEG

shell under pH 6.5 because the Phe could not be protonated. DCFH-DA was chosen as the ROS fluorescent probe to determine intracellular ROS generation. The results showed that no ROS was detected in the PBS with or without laser irradiation group, indicating laser irradiation itself could not affect ROS generation. With the presence of MMP-2 (+E) and laser irradiation (+L), PEG-His@BPC + E + L group showed strongest ROS fluorescence, implying that the transformation from spherical nanoparticles to nanofibers could obviously improve the ability to generate ROS, which was due to enhanced intracellular retention capacity (Fig. 3A). Moreover, there was no detectable ROS in the Ce6 group, but a small amount of ROS was detected in PEG-His@BPC group and PEG-Phe@BPC group. This result implied that BBR also had the ability to produce ROS, which was consistent with previous reports[39]. In order to further prove the ability of BBR to produce ROS, we synthesized PEG-His@Arg-PLGVRKLVFF-Ce6 (PEG-His@APC) that was without BBR. As we expected, the results showed that PEG-His@BPC + L group could generate more ROS than PEG-His@APC + L group, and there was no ROS in PEG-His@APC group, indicating BBR could indeed generate ROS (Fig. 3B). Therefore, the generation of ROS could further magnify when Ce6 and BBR were used in the tumor treatment together, which could establish a good theoretical foundation for the combination therapy of PDT and chemotherapy.

3.7. *Cytotoxicity analysis*

In order to elucidate the relationship between incubation concentration of drugs and cytotoxicity and select the appropriate administration concentration, MTT assays were carried out (Fig. 4B). After laser irradiation, the toxicity increased obviously when the concentration of Ce6 was above 4 μg/mL, which was consistent with previous reports[40]. Moreover, the PEG-His@BPC + E + L showed obvious cytotoxicity with lowest half-maximal inhibitory concentration value (IC_{50}) among all groups, indicating that shape transformable nanoparticles could enhance the cytotoxicity. In order to further investigate the antitumor effect at cellular level, the Calcein−AM/PI double staining was performed (Fig. 4A). The results showed that all the cells in the PBS group survived regardless of laser irradiation, indicating that laser irradiation alone did not lead to cell death. However, a small number of dead cells were observed in PEG-His@BPC + E group, which ascribed to the presence of BBR. After laser irradiation, due to the large amount of ROS generated by Ce6, the toxicity of each group had a corresponding increase. It could be found that the cytotoxicity of PEG-His@BPC + E + L group was the strongest, which induced almost 100% of cell death. These results indicated that the shape transformable nanoparticles with chemo-photodynamic therapy achieved the remarkable cytotoxicity, which was consistent with the previous results of ROS generation experiment. In addition, it had been reported that both BBR and Ce6 could promote apoptosis[41−45]. In order to further investigate the effect of PEG-His@BPC on apoptosis promoting, PI/Annexin V−FITC double staining experiment was carried out. The results showed that free BBR and Ce6+L could induce early apoptosis by 9.91 ± 0.52% and 26.70 ± 2.67% and late apoptosis by 21.16 ± 2.93% and 24.08 ± 2.02%, respectively. In addition, PEG-His@BPC + E + L reached the best degree of apoptosis among all formulations, even higher than that of free Ce6+L, resulting in 34.32 ± 3.13% of early apoptosis and 40.25 ± 3.52% of late apoptosis, respectively. Compared with PBS group, PEG-His@BPC + E + L group increased early apoptosis by 29.72% and late apoptosis by 33.94%, respectively (Fig. 4C and D). These results jointly demonstrated that the shape transformable

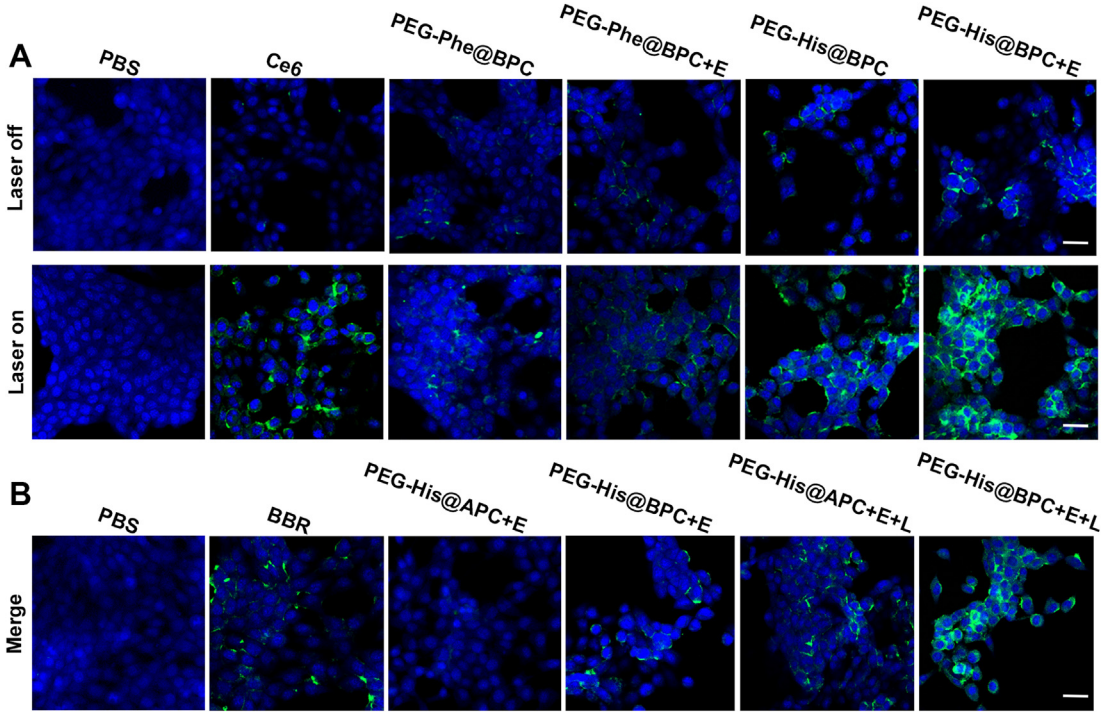

Figure 3 Chemo-photodynamic therapy on 4T1 cells. (A) Detection of ROS generated by various formulations at cell level. (B) Verification of the capacity of BBR to generate ROS. Blue represents nuclei, green represents ROS, and scale bars represent 100 μm. The concentration of Ce6 is 5 μg/mL, and the concentration of BBR is 3 μg/mL in ROS experiment. E and L represent MMP-2 and laser irradiation, respectively.

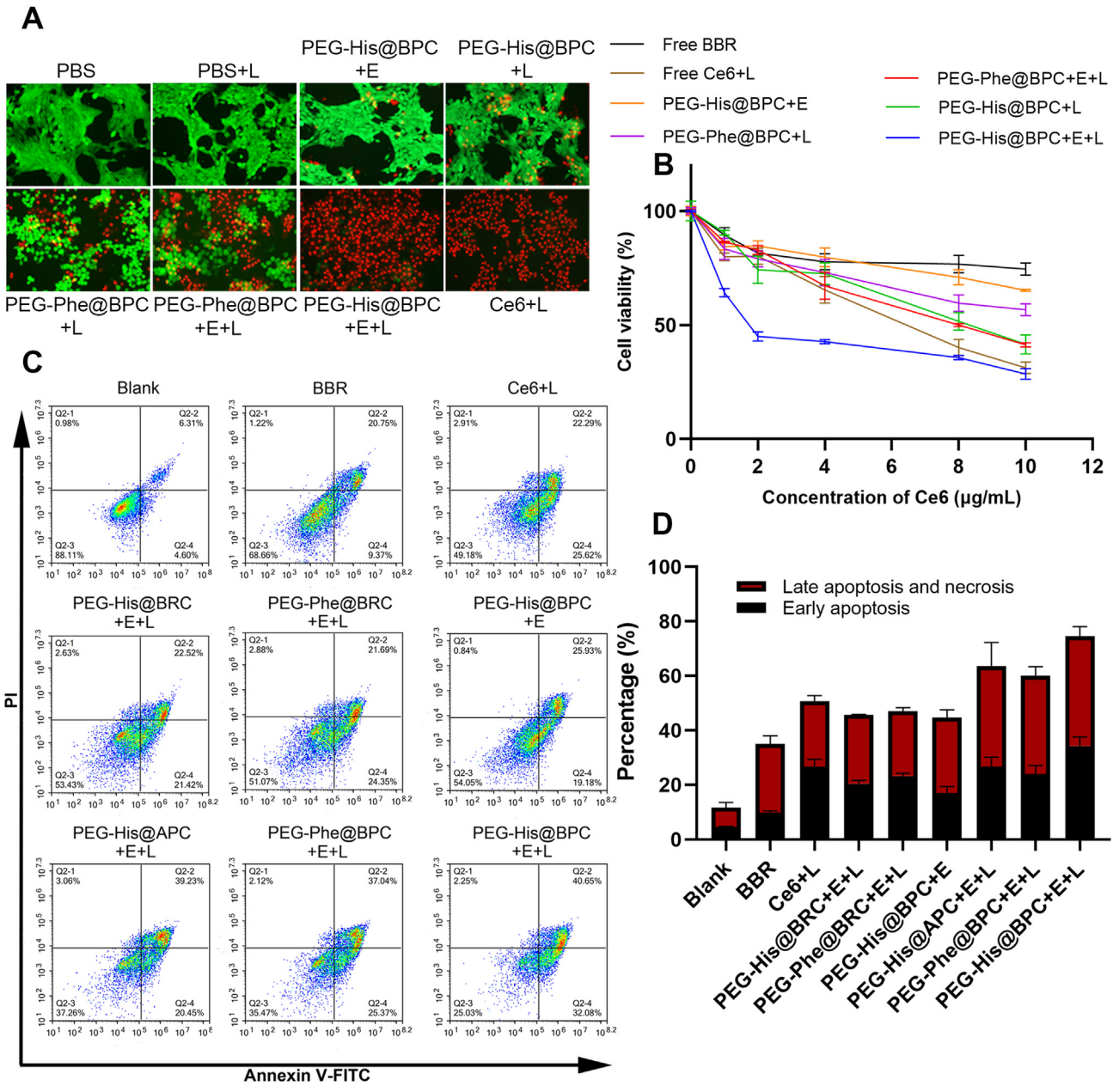

Figure 4 (A) Calcein−AM/PI double staining of cells treated with different formulations. Calcein−AM represents live cells and PI represents dead cells, and the concentration of Ce6 is 5 μg/mL. (B) MTT assay after incubating 4T1 cells with different formulations for 24 h. Data are presented as mean ± SD (n = 6). (C, D) 4T1 cell apoptosis assay with different formulations that determined by flow cytometry (Agilent). The concentration of Ce6 is 2 μg/mL. Data are presented as mean ± SD (n = 3).

nanoparticles with chemo-photodynamic therapy could achieve the best effect of apoptosis. This was consistent with the above results of ROS experiment and MTT, indicating the strategy of shape transformable nanoparticles with combination therapy showed strong therapeutic effect.

3.8. *In vivo targeting evaluation*

In order to evaluate the tumor targeting capacity of the nanomedicines in 4T1 breast tumor models, unresponsive PEG-Phe@BBR-RPGFGNKLVFF-Ce6 (PEG-Phe@BRC), pH-responsive PEG-His@BRC, MMP-2-responsive PEG-Phe@BPC and dual-responsive PEG-His@BPC were constructed. The changes of fluorescence signals *in vivo* were observed at 4, 12, 24, 36 and 48 h after intravenous injection by *in vivo* fluorescence imaging system (PerkinElmer, Fig. 5A). Four kinds of nanoparticles were widely distributed throughout the body at 4 h, regardless of whether they could respond to tumor microenvironment or not. Importantly, PEG-His@BPC and PEG-Phe@BPC could accumulate at the tumor site in 48 h, while the fluorescence signal of PEG-His@BRC and PEG-Phe@BRC showed a trend of rapid clearance after 24 h, indicating that shape transformable nanoparticles could be more prone to accumulate at tumor site. The tumor fluorescence signal of PEG-His@BPC was slightly stronger than that of PEG-Phe@BPC at 24 h, confirming that charge reversible strategy could enable nanoparticles to accumulate at tumor site more easily. According to

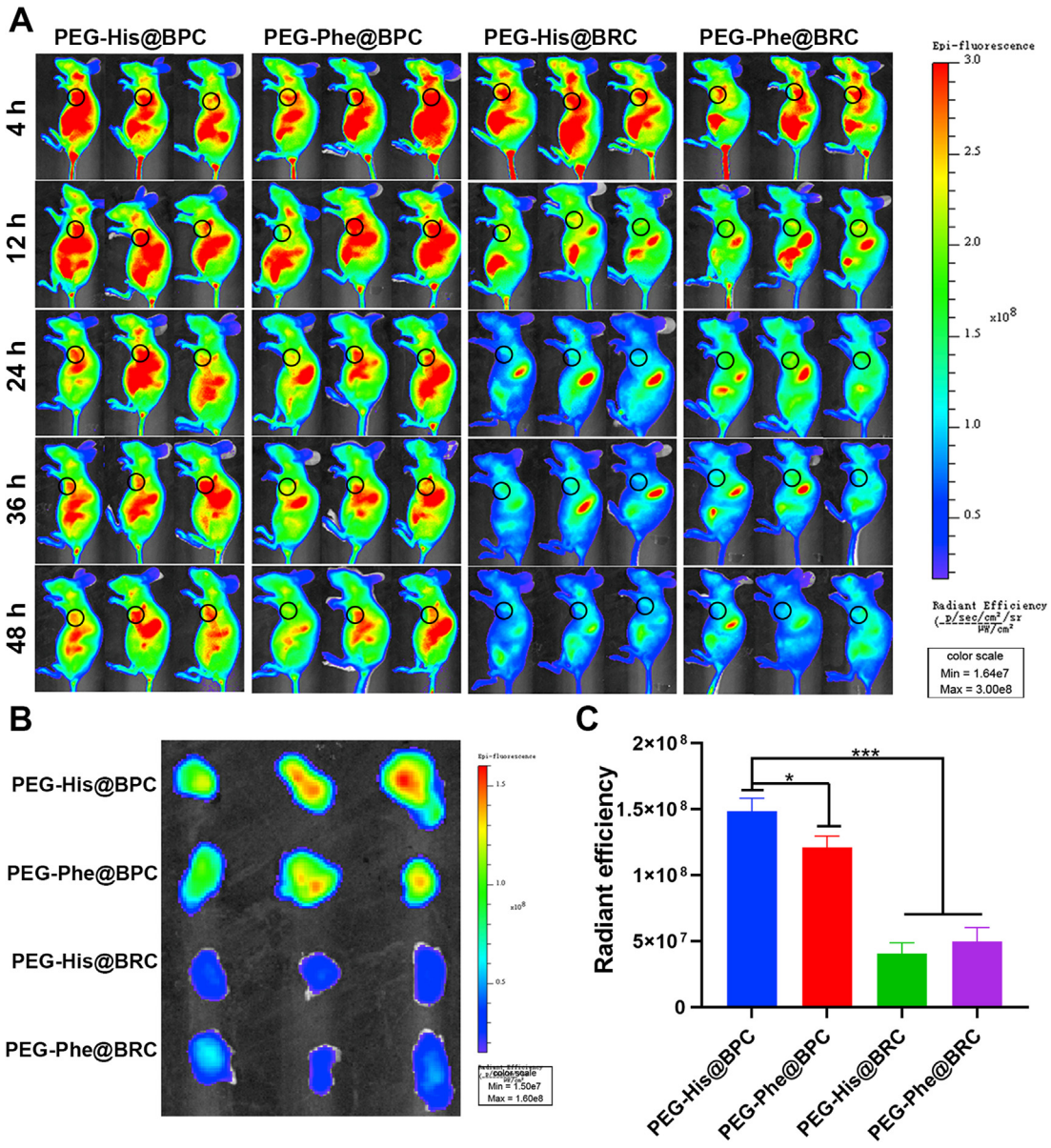

Figure 5 (A) *In vivo* fluorescent imaging of mice with different intravenous treatments at 4, 12, 24, 36, and 48 h. The black circles represent the locations of tumors. *Ex vivo* fluorescent imaging of tumors at 48 h (B) and their semi-quantification (C). The unit of color scales and radiant efficiency is [p/sec/cm^2/sr]/[μW/cm^2]. Data are presented as mean ± SD (n = 3). *P < 0.05 and ***P < 0.001 are considered as significant difference.

the *ex vivo* imaging of major organs and tumors at 48 h (Supporting Information Fig. S5A and S5B) and semi-quantitative results (Fig. S5B and S5C), the tumor fluorescence intensity of PEG-His@BPC was 1.2, 3.5, and 2.9 times higher than that of PEG-Phe@BPC, PEG-His@BRC and PEG-Phe@BRC, respectively. All the above results showed that the dual-responsive nanoparticles with transformable shape and reversible charge could effectively enhance the tumor targeting *in vivo*, which was very important for the follow-up treatment effect and consistent with the previous reports[46].

3.9. *In vivo retention evaluation*

In order to further confirm the tumor retention of shape-transformed nanoparticles *in vivo*, PEG-His@BPC, PEG-Phe@BPC, PEG-His@BRC and PEG-Phe@BRC were intratumorally injected into mice with the same tumor size. Then, the intratumoral fluorescence signals were captured at 0, 8, 12, 24 and 36 h, respectively (Fig. 6A and B). The results showed that the intratumoral fluorescence signals of all groups were strong and similar at the initial time point. However, at 24 h, the intratumoral fluorescence signals of the PEG-His@BRC and PEG-Phe@BRC almost disappeared, while the intratumoral fluorescence signals of the PEG-His@BPC and PEG-Phe@BPC still maintained a very high level, and the intratumoral intensity of PEG-His@BPC was 1.79, 1.99 and 1.36 times higher than that of PEG-His@BRC, PEG-Phe@BRC and PEG-Phe@BPC, respectively. These results confirmed that transformable shape could enable nanoparticles more prone to retain at tumor site. The *in vivo* imaging results were consistent with the *ex vivo*

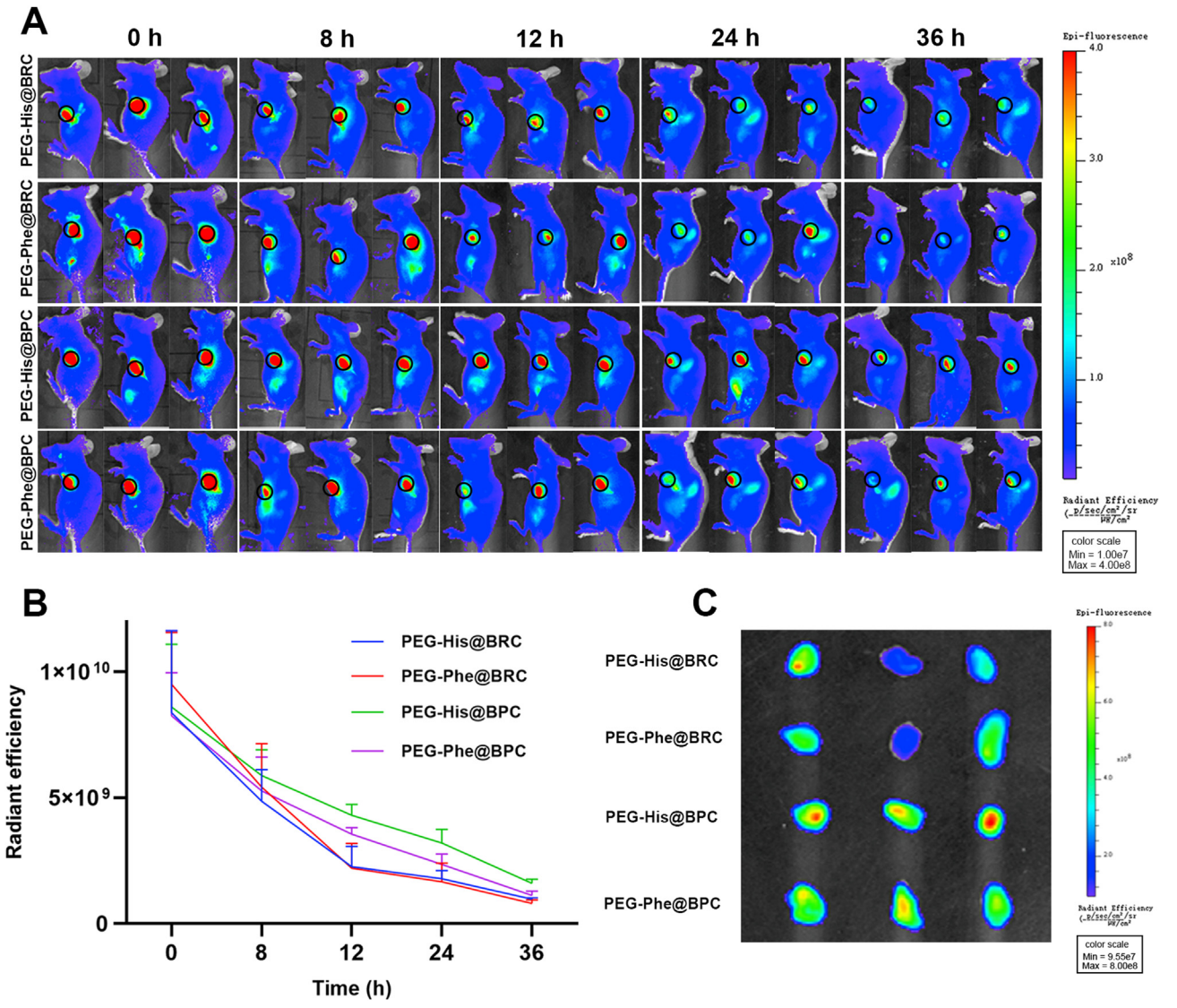

Figure 6 (A) *In vivo* fluorescent imaging of mice at 0, 8, 12, 24, and 36 h after intratumoral injection with different formulations. The black circles represent the locations of tumors. (B) Changes in intratumoral fluorescent intensity at different time points. Data are presented as mean ± SD ($n = 3$). (C) *Ex vivo* fluorescent imaging of tumors at 36 h.

results (Fig. 6C). In order to further confirm that the enhanced tumor retention was due to the shape transformation of PEG-His@BPC, TEM (JEOL) was utilized to analyze the nanomaterials at the tumor site. Result showed that the PEG-His@BRC maintained a spherical structure in the tumor, while many nanofibers were found in the tumor treated with PEG-His@BPC (Supporting Information Fig. S6A and S6B), indicating that the enhanced tumor retention of PEG-His@BPC was due to the transformation to nanofibers.

3.10. Anti-tumor effect in vivo

Inspired by *in vitro* toxicity test and *in vivo* tumor targeting and tumor retention evaluation, the *in vivo* anti-tumor effect was evaluated. The results showed that the average tumor volume of PBS group, Ce6+L group, BBR group and PEG-His@BPC group increased rapidly, which was higher than 800 mm^3 on Day 22 (Fig. 7A–D). However, PEG-Phe@BPC + L, PEG-His@BRC + L, PEG-Phe@BRC + L and PEG-His@APC + L groups showed slower growth rates (Fig. 7E–I), and the PEG-His@BPC + L group showed the smoothest growth curve. The average tumor volume of PEG-His@BPC group only reached 289 mm^3 (Fig. 7J). Compared with the PBS group on Day 22, the tumor inhibition rates of PEG-His@BPC, PEG-Phe@BPC, PEG-His@BRC, PEG-Phe@BRC and PEG-His@APC were 71.4%, 49.5%, 27.2%, 23.0% and 46.3%, respectively. The results indicated the dual-responsive nanoparticles with transformable shape and reversible charge could obviously enhance the therapeutic effect against tumor. The body weight of mice in each group did not change much (Fig. 7K). The results of tumor image and tumor weight under natural light were in line with the previous measurements (Fig. 7L and Supporting Information Fig. S7). The images of hematoxylin and eosin (H&E) staining sections showed that there were no obvious histological changes in the main organs (Supporting Information Fig. S8). TUNEL staining and Ki67 staining showed that PEG-His@BPC had the best capacity to promote tumor apoptosis

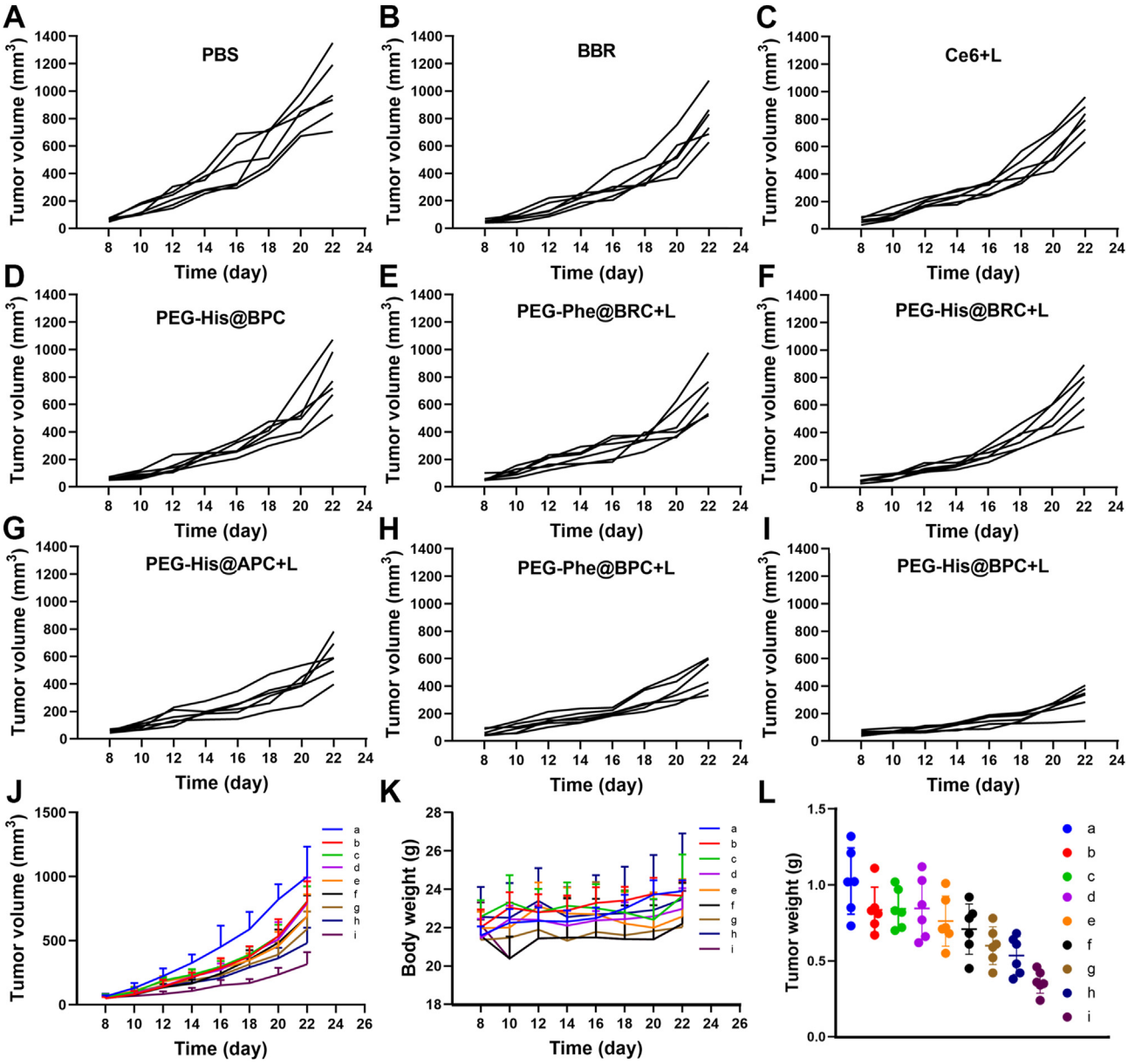

Figure 7 (A–I) Tumor volume of each mouse in the groups treated with (A) PBS, (B) BBR, (C) Ce6+L, (D) PEG-His@BPC, (E) PEG-Phe@BRC + L, (F) PEG-His@BRC + L, (G) PEG-His@APC + L, (H) PEG-Phe@BPC + L, (I) PEG-His@BPC + L. (J) Tumor volume, (K) body weights and (L) tumor weights of different treatment groups. The a–i represent PBS, BBR, Ce6+L, PEG-His@BPC, PEG-Phe@BRC + L, PEG-His@BRC + L, PEG-His@APC + L, PEG-Phe@BPC + L and PEG-His@BPC + L, respectively. Data are presented as mean ± SD ($n = 6$).

(Supporting Information Fig. S9A and S9B). The blood biochemical data also showed that the liver and kidney tissue function of each group was normal and there was no obvious toxicity (Fig. S9C–S9G). These results jointly demonstrated that PEG-His@BPC not only amplified chemo-photodynamic therapy of breast cancer through the combination of shape transformation and charge reversal, but also had low toxicity to normal organs.

4. Conclusions

Herein, we reported a new type of dual-responsive nanoparticles (PEG-His@BPC) with shape transformation, reversible charge and chemo-photodynamic therapy. First, the negatively charged spherical PEG-His@BPC had long circulation time in the blood. When the PEG-His@BPC reached the tumor site through the EPR effect, the PEG shell fell off triggered by the acidic tumor microenvironment, resulting in charge reversal and exposure of the enzyme cutting site. The positive charge of the BPC was conducive to the tumor penetration. When the BPC penetrated into the deep tumor, BBR was released to promote apoptosis and the spherical BPC transformed into nanofibers, which could enhance the tumor retention. The shape transformation and its effect were confirmed by *in vitro* and *in vivo* analysis. In addition, PEG-His@BPC successfully amplified chemo-photodynamic therapy

of breast cancer through the combination of shape transformation and charge reversal. In general, these studies have proved that this nanosystem was very promising in therapy of breast cancer.

The future research direction of dual-responsive nanoparticles with transformable shape and reversible charge should try to treat breast cancer brain metastases (BCBMs), which are cause of morbidity and mortality among patients with breast cancer[47,48]. Systemic drug therapy is usually effective for peripheral breast cancer, but it is often ineffective for BCBM because of poor penetration to the blood−brain barrier (BBB)[49−51]. Some studies have shown that the shape of nanoparticles has obvious effect on the penetration to BBB, which suggested that altering the shape of nanocarriers could influence their uptake into the brain, whereby increasing the efficacy and bioavailability of therapeutic agents[52−54]. Moreover, a variety of strategies or nanoparticles have been found to improve the penetration to BBB[55], such as the strategy of escaping from abluminal LRP1-mediated clearance[56], PSMA-targeted nanoparticles[57], LRP1-upregulated nanoparticles[58]. Combining shape transformable nanoparticles with above strategies or nanoparticles to overcome the BBB may be a new direction for defeating BCBM.

Acknowledgments

The work was supported by National Natural Science Foundation of China (82173762), 111 Project (B18035, China), the Key Research and Development Program of Science and Technology Department of Sichuan Province (2022JDJQ0050, 2022YFS0334), and the Open Research Fund of Chengdu University of Traditional Chinese Medicine State Key Laboratory of Characteristic Chinese Medicine Resources in Southwest China. We would like to thank the Analytical & Testing Center of Sichuan University for TEM (Meiju Xie) work.

Author contributions

Huile Gao and Rui Liu designed the research. Wenfeng Jia, Rui Liu and Yushan Wang carried out the experiments and performed data analysis. Wenfeng Jia wrote the manuscript and Wenqi Yu, Chuan Hu, Yang Zhou, Ling Wang, Mengjiao Zhang and Xiang Gao assisted writing. All of the authors have read and approved the final manuscript.

Conflicts of interest

The authors declare no conflicts of interest.

Appendix A. Supporting information

Supporting data to this article can be found online at https://doi.org/10.1016/j.apsb.2022.03.010.

References

1. Whiteside TL. The tumor microenvironment and its role in promoting tumor growth. *Oncogene* 2008;**27**:5904−12.
2. Wang S, Huang P, Chen XY. Hierarchical targeting strategy for enhanced tumor tissue accumulation/retention and cellular internalization. *Adv Mater* 2016;**28**:7340−64.
3. Yang S, Gao HL. Nanoparticles for modulating tumor microenvironment to improve drug delivery and tumor therapy. *Pharmacol Res* 2017;**126**:97−108.
4. Zhou Y, Chen XC, Cao J, Gao HL. Overcoming the biological barriers in the tumor microenvironment for improving drug delivery and efficacy. *J Mater Chem B* 2020;**8**:6765−81.
5. Stohrer M, Boucher Y, Stangassinger M, Jain RK. Oncotic pressure in solid tumors is elevated. *Cancer Res* 2000;**60**:4251−5.
6. Liu R, An Y, Jia WF, Wang YS, Wu Y, Zhen YH, et al. Macrophage-mimic shape changeable nanomedicine retained in tumor for multimodal therapy of breast cancer. *J Control Release* 2020;**321**:589−601.
7. Luo HH, Kong L, Zhang F, Huang CL, Chen JY, Zhang HB, et al. Light-controlled nanosystem with size-flexibility improves targeted retention for tumor suppression. *Adv Funct Mater* 2021;**31**:2101262.
8. Yu WQ, Hu C, Gao HL. Intelligent size-changeable nanoparticles for enhanced tumor accumulation and deep penetration. *ACS Appl Bio Mater* 2020;**3**:5455−62.
9. Yu WQ, Liu R, Zhou Y, Gao HL. Size-tunable strategies for a tumor targeted drug delivery system. *ACS Cent Sci* 2020;**6**:100−16.
10. Jia WF, Wang YS, Liu R, Yu XR, Gao HL. Shape transformable strategies for drug delivery. *Adv Funct Mater* 2021;**31**:2009765.
11. Xiao W, Gao HL. The impact of protein corona on the behavior and targeting capability of nanoparticle-based delivery system. *Int J Pharm* 2018;**552**:328−39.
12. Xu FJ. Deciphering the impact of PEG antifouling layer on surface attached functional peptides in regulating cell behaviors. *Chin Chem Lett* 2019;**30**:2051−2.
13. Bellat V, Ting R, Southard TL, Vahdat L, Molina H, Fernandez J, et al. Functional peptide nanofibers with unique tumor targeting and enzyme-induced local retention properties. *Adv Funct Mater* 2018;**28**:1803969.
14. Han K, Zhang J, Zhang WY, Wang SB, Xu LM, Zhang C, et al. Tumor-triggered geometrical shape switch of chimeric peptide for enhanced *in vivo* tumor internalization and photodynamic therapy. *ACS Nano* 2017;**11**:3178−88.
15. Lin CC, Tong F, Liu R, Xie R, Lei T, Chen YX, et al. GSH-responsive SN38 dimer-loaded shape-transformable nanoparticles with iRGD for enhancing chemo-photodynamic therapy. *Acta Pharm Sin B* 2020;**10**:2348−61.
16. Saleh T, Kalodimos CG. Enzymes at work are enzymes in motion. *Science* 2017;**355**:247−8.
17. Godefroy E, Guilloux Y, Jotereau F, Bhardwaj N. MMP-2: a novel target for antitumor immune therapy. *J Clin Oncol* 2009;**27**:3053.
18. Lei Q, Qiu WX, Hu JJ, Cao PX, Zhu CH, Cheng H, et al. Multifunctional mesoporous silica nanoparticles with thermal-responsive gatekeeper for NIR light-triggered chemo/photothermal-therapy. *Small* 2016;**12**:4286−98.
19. Zhang J, Yuan ZF, Wang Y, Chen WH, Luo GF, Cheng SX, et al. Multifunctional envelope-type mesoporous silica nanoparticles for tumor-triggered targeting drug delivery. *J Am Chem Soc* 2013;**135**:5068−73.
20. Ma MM, Liu ZQ, Gao N, Pi ZF, Du XB, Ren JS, et al. Self-protecting biomimetic nanozyme for selective and synergistic clearance of peripheral amyloid-beta in an Alzheimer's disease model. *J Am Chem Soc* 2020;**142**:21702−11.
21. Wood SJ, Wetzel R, Martin JD, Hurle MR. Prolines and amyloidogenicity in fragments of the Alzheimer's peptide beta/A4. *Biochemistry* 1995;**34**:724−30.
22. Mei H, Cai SS, Huang D, Gao HL, Cao J, He B. Carrier-free nanodrugs with efficient drug delivery and release for cancer therapy: from intrinsic physicochemical properties to external modification. *Bioact Mater* 2021;**8**:220−40.
23. Wei JP, Li JC, Sun D, Li Q, Ma JY, Chen XL, et al. A novel theranostic nanoplatform based on Pd@Pt-PEG-Ce6 for enhanced photodynamic therapy by modulating tumor hypoxia microenvironment. *Adv Funct Mater* 2018;**28**:1706310.
24. Bhadra K, Kumar GS. Therapeutic potential of nucleic acid-binding isoquinoline alkaloids: binding aspects and implications for drug design. *Med Res Rev* 2011;**31**:821−62.
25. Hu J, Yuan XW, Wang F, Gao HL, Liu XL, Zhang W. The progress and perspective of strategies to improve tumor penetration of nanomedicines. *Chin Chem Lett* 2021;**32**:1341−7.

26. Zhou Q, Shao SQ, Wang JQ, Xu CH, Xiang JJ, Piao Y, et al. Enzyme-activatable polymer-drug conjugate augments tumour penetration and treatment efficacy. *Nat Nanotechnol* 2019;**14**:799−809.
27. Wang HX, Zuo ZQ, Du JZ, Wang YC, Sun R, Cao ZT, et al. Surface charge critically affects tumor penetration and therapeutic efficacy of cancer nanomedicines. *Nano Today* 2016;**11**:133−44.
28. Liu SW, Wang L, Zhang MS, Tao KP, Wang B, Lin M, et al. Tumor microenvironment-responsive nanoshuttles with sodium citrate modification for hierarchical targeting and improved tumor theranostics. *ACS Appl Mater Interfaces* 2019;**11**:25730−9.
29. Zhou L, Du C, Zhang R, Dong CM. Stimuli-responsive dual drugs-conjugated polydopamine nanoparticles for the combination photothermal-cocktail chemotherapy. *Chin Chem Lett* 2021;**32**:561−4.
30. Song Y, Jing H, Vong LB, Wang J, Li N. Recent advances in targeted stimuli-responsive nano-based drug delivery systems combating atherosclerosis. *Chin Chem Lett* 2021;**33**:1705−33.
31. Hu C, Cun XL, Ruan SB, Liu R, Xiao W, Yang XT, et al. Enzyme-triggered size shrink and laser-enhanced NO release nanoparticles for deep tumor penetration and combination therapy. *Biomaterials* 2018;**168**:64−75.
32. Xiong JY, Gao HL. Matrix metalloproteases-responsive nanomaterials for tumor targeting diagnosis and treatment. *J Microencapsul* 2017;**34**:440−53.
33. Soto C, Sigurdsson EM, Morelli L, Kumar RA, Castano EM, Frangione B. Beta-sheet breaker peptides inhibit fibrillogenesis in a rat brain model of amyloidosis: implications for Alzheimer's therapy. *Nat Med* 1998;**4**:822−6.
34. Xu CF, Yu YL, Sun Y, Kong L, Yang CL, Hu M, et al. Transformable nanoparticle-enabled synergistic elicitation and promotion of immunogenic cell death for triple-negative breast cancer immunotherapy. *Adv Funct Mater* 2019;**29**:1905213.
35. Sun JS, Zhang L, Wang JL, Feng Q, Liu DB, Yin QF, et al. Tunable rigidity of (polymeric core)−(lipid shell) nanoparticles for regulated cellular uptake. *Adv Mater* 2015;**27**:1402−7.
36. Liu R, Yu MN, Yang XT, Umeshappa CS, Hu C, Yu WQ, et al. Linear chimeric triblock molecules self-assembled micelles with controllably transformable property to enhance tumor retention for chemo-photodynamic therapy of breast cancer. *Adv Funct Mater* 2019;**29**:1808462.
37. Tang L, Yang X, Yin Q, Cai K, Wang H, Chaudhury I, et al. Investigating the optimal size of anticancer nanomedicine. *Proc Natl Acad Sci U S A* 2014;**111**:15344−9.
38. Popovic Z, Liu W, Chauhan VP, Lee J, Wong C, Greytak AB, et al. A nanoparticle size series for *in vivo* fluorescence imaging. *Angew Chem Int Ed Engl* 2010;**49**:8649−52.
39. Zhu XF, Yue HD, Guo XF, Yang JY, Liu JS, Liu JT, et al. The preconditioning of berberine suppresses hydrogen peroxide-induced premature senescence *via* regulation of Sirtuin 1. *Oxid Med Cell Longev* 2017;**2017**:2391820.
40. Qin Y, Tong F, Zhang W, Zhou Y, He SQ, Xie R, et al. Self-delivered supramolecular nanomedicine with transformable shape for ferrocene-amplified photodynamic therapy of breast cancer and bone metastases. *Adv Funct Mater* 2021;**31**:2104645.
41. Tong HX, Chen YJ, Li ZH, Li H, Chen TT, Jin Q, et al. Glutathione activatable photosensitizer-conjugated pseudopolyrotaxane nanocarriers for photodynamic theranostics. *Small* 2016;**12**:6223−32.
42. Hyun MS, Hur JM, Mun YJ, Kim D, Woo WH. BBR induces apoptosis in *HepG2* cell through an Akt-ASK1-ROS-p38MAPKs-linked cascade. *J Cell Biochem* 2010;**109**:329−38.
43. Zheng F, Tang Q, Wu JJ, Zhao SY, Liang ZY, Li LN, et al. *p38*alpha MAPK-mediated induction and interaction of FOXO3a and p53 contribute to the inhibited-growth and induced-apoptosis of human lung adenocarcinoma cells by berberine. *J Exp Clin Cancer Res* 2014;**33**:36.
44. Zhao YW, Jing ZL, Lv J, Zhang ZW, Lin JT, Cao XJ, et al. Berberine activates caspase-9/cytochrome c-mediated apoptosis to suppress triple-negative breast cancer cells *in vitro* and *in vivo*. *Biomed Pharmacother* 2017;**95**:18−24.
45. Yu L, Wang ZJ, Mo ZM, Zou BH, Yang YY, Sun R, et al. Synergetic delivery of triptolide and Ce6 with light-activatable liposomes for efficient hepatocellular carcinoma therapy. *Acta Pharm Sin B* 2021;**11**:2004−15.
46. Xu CF, Sun Y, Yu YL, Hu M, Yang CL, Zhang ZP. A sequentially responsive and structure-transformable nanoparticle with a comprehensively improved 'CAPIR cascade' for enhanced antitumor effect. *Nanoscale* 2019;**11**:1177−94.
47. Li J, Cai P, Shalviri A, Henderson JT, He C, Foltz WD, et al. A multifunctional polymeric nanotheranostic system delivers doxorubicin and imaging agents across the blood−brain barrier targeting brain metastases of breast cancer. *ACS Nano* 2014;**8**:9925−40.
48. Yu WQ, Hu C, Gao HL. Advances of nanomedicines in breast cancer metastasis treatment targeting different metastatic stages. *Adv Drug Deliv Rev* 2021;**178**:113909.
49. Tsao MN, Rades D, Wirth A, Lo SS, Danielson BL, Gaspar LE, et al. Radiotherapeutic and surgical management for newly diagnosed brain metastasis(es): an American Society for Radiation Oncology evidence-based guideline. *Pract Radiat Oncol* 2012;**2**:210−25.
50. Connell JJ, Chatain G, Cornelissen B, Vallis KA, Hamilton A, Seymour L, et al. Selective permeabilization of the blood−brain barrier at sites of metastasis. *J Natl Cancer Inst* 2013;**105**:1634−43.
51. Ruan SB, Zhou Y, Jiang XG, Gao HL. Rethinking CRITID procedure of brain targeting drug delivery: circulation, blood−brain barrier recognition, intracellular transport, diseased cell targeting, internalization, and drug release. *Adv Sci* 2021;**8**:2004025.
52. Glangchai LC, Caldorera-Moore M, Shi L, Roy K. Nanoimprint lithography based fabrication of shape-specific, enzymatically-triggered smart nanoparticles. *J Control Release* 2008;**125**:263−72.
53. Kolhar P, Anselmo AC, Gupta V, Pant K, Prabhakarpandian B, Ruoslahti E, et al. Using shape effects to target antibody-coated nanoparticles to lung and brain endothelium. *Proc Natl Acad Sci U S A* 2013;**110**:10753−8.
54. Lee C, Hwang HS, Lee S, Kim B, Kim JO, Oh KT, et al. Rabies virus-inspired silica-coated gold nanorods as a photothermal therapeutic platform for treating brain tumors. *Adv Mater (Weinheim, Ger)* 2017;**29**:1605563.
55. Gao HL. Progress and perspectives on targeting nanoparticles for brain drug delivery. *Acta Pharm Sin B* 2016;**6**:268−86.
56. Khan NU, Ni J, Ju XF, Miao TT, Chen HY, Han L. Escape from abluminal LRP1-mediated clearance for boosted nanoparticle brain delivery and brain metastasis treatment. *Acta Pharm Sin B* 2021;**11**:1341−54.
57. Ni J, Miao T,T, Su M, Khan NU, Ju XF, Chen HY, et al. PSMA-targeted nanoparticles for specific penetration of blood−brain tumor barrier and combined therapy of brain metastases. *J Control Release* 2021;**329**:934−47.
58. Guo Q, Zhu QN, Miao TT, Tao J, Ju XF, Sun ZL, et al. LRP1-upregulated nanoparticles for efficiently conquering the blood−brain barrier and targetedly suppressing multifocal and infiltrative brain metastases. *J Control Release* 2019;**303**:117−29.